Supporting Information

Adhesion of 2D MoS_2 to Graphite and Metal Substrates Measured by a Blister Test

Metehan Calis[1], David Lloyd[2], Narasimha Boddeti[3], and J. Scott Bunch[1,4*]

[1]Boston University, Department of Mechanical Engineering, Boston, MA 02215 USA

[2]Analog Garage, Analog Devices Inc, Boston, MA 02110 USA

[3]Washington State University, School of Mechanical and Materials Engineering, WA 99163 USA

[4]Boston University, Division of Materials Science and Engineering, Brookline, MA 02446 USA

*e-mail: bunch@bu.edu

1. Growth and Characterization

We used chemical vapor deposition (CVD) to grow monolayer MoS_2 flakes[1,2] (Fig. S1a). Initially, MoS_2 powder (Thermo Fisher Scientific, Molybdenum (IV) sulfide, 98%) is placed into the middle of the furnace inside an aluminum oxide crucible. A SiO_x wafer, which is cleaned with acetone, isopropyl alcohol (IPA), and deinozied (DI) water and then exposed to ultraviolet (UV) for 5 minutes, is placed into a cooler region downstream of the MoS_2 powder. Before starting the growth, the furnace is put under vacuum and purged with Argon (200 sccm) to remove air (specifically O_2). We then introduce 60 sccm Ar, 0.06 sccm O_2, and 1.8 sccm H_2 inside the tube. The growth process consists of three steps: (i) heating up to 900 ^oC for 15 minutes, (ii) holding at 900 ^oC for 15 minutes, and (iii) cooling the furnace to room temperature. During the growth, MoS_2 powder sublimates and is carried downstream by Ar gas where it condenses onto the cooler SiO_x substrate.

After the growth, we observe numerous monolayer flakes in the optical microscope with ~ 100 μm side length. We deduce the approximate number of layers by using optical contrast[3] and confirm this with both Raman spectroscopy (Fig. S1b) and photoluminescence (PL) spectroscopy (Fig. S1c). Both Raman and PL Spectroscopy were conducted in a Renishaw Raman InVia microscope using a 532 nm laser beam with 1200 l/mm gratings. In Raman spectroscopy, we obtained two prominent resonances[4], the in-plane (E^1_{2g}) and out-of-plane (A_{1g}) vibrations located at 385 cm^{-1} and 405 cm^{-1} respectively, consistent with monolayer flakes. PL measurements[5] show a peak at 1.9 eV (A exciton) and the absence of an indirect peak, both indicative of monolayer MoS_2.

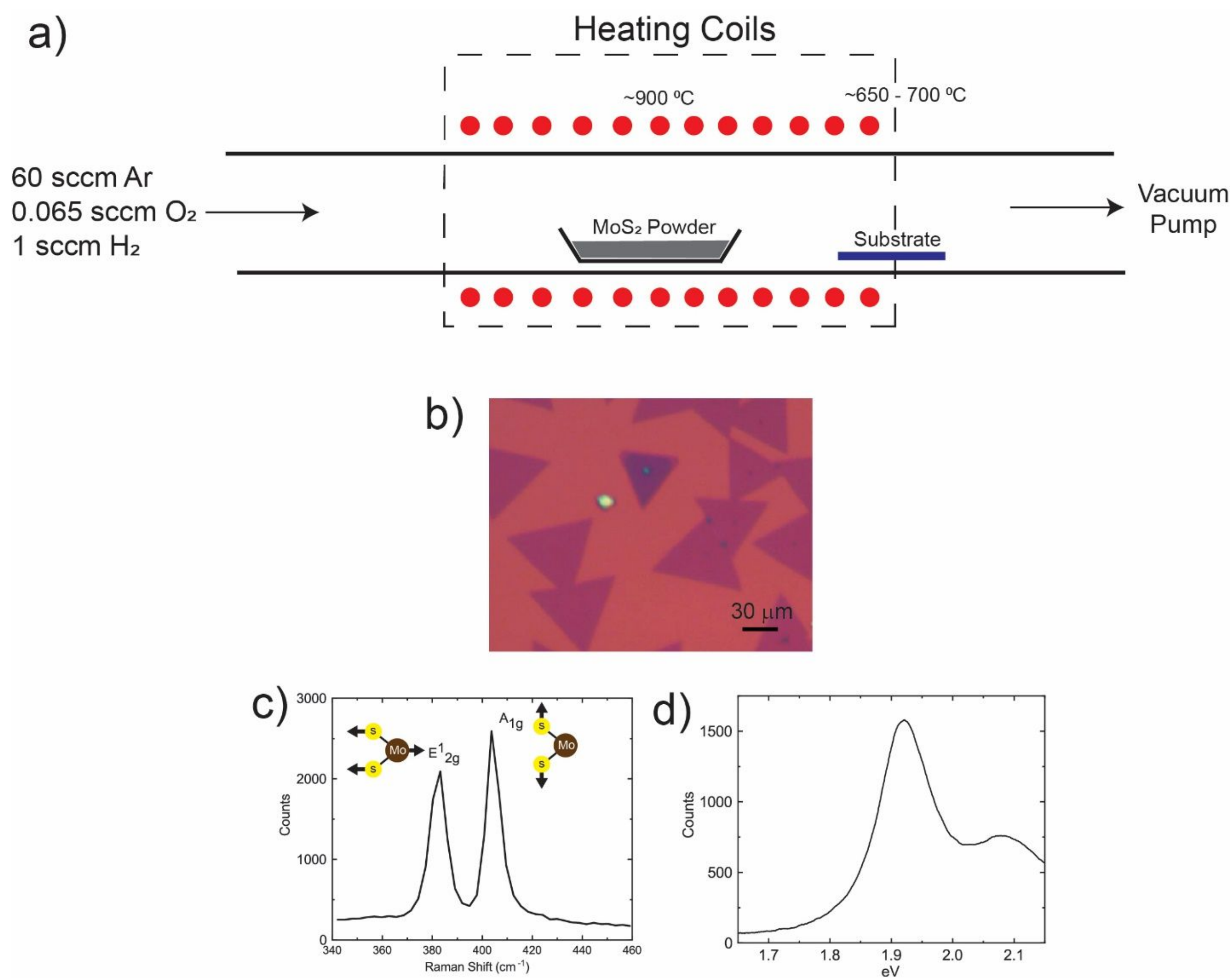

Figure S1. a) Schematics of the positions of the crucible and substrate in the furnace. **b)** Monolayer MoS_2 flakes on the SiO_x substrate after the growth. **c)** Raman spectrum (Inset: Schematic of vibrational modes, E^1_{2g} and A_{1g}). **d)** PL spectrum.

2. Metal Substrate Fabrication

Here we describe briefly the steps of the fabrication of the metal substrates. First, we clean the SiO_x chips with acetone, IPA, and DI water. The surface of the SiO_x is spin-coated with a photoresist solution of S1818 at 2500 rpm, and the substrate is put on a hot plate at 115 ^{o}C for 1 minute. We use a contact aligner with a mask with 5 μm diameter circles on it to create the photoresist pattern. The spin-coated chips are exposed to UV for 20 seconds with 8 mW power. The parts which are exposed to UV are removed with MF-319 Developer and then SiO_x and Si are etched by Reactive-Ion-Etching (RIE). We use 3.1 sccm O_2 and 25 sccm CF_4 at 100 mTorr pressure and 150 W power for 13 minutes of etching. This creates wells with a depth between ~ 600-900 nm. In the final step, we remove the photoresist, in a bath of 1165 Remover where the chip soaks for 12 hours at 110 ^{o}C. To further clean the chips of photoresist residue, we put the etched wells into an O_2 plasma at 300 Watts with 300 sccm of O_2 for 2 minutes. The microcavities are then placed into a thermal evaporator. Germanium, Chromium, and Titanium are evaporated over the etched well with a thickness of 300 Å and a rate of 0.5 Å/s. For the gold substrate, 180 Å-thick Titanium is used as an adhesive and 450 Å of gold is subsequently evaporated. A similar process is utilized for the other metals studied (Fig. S2).

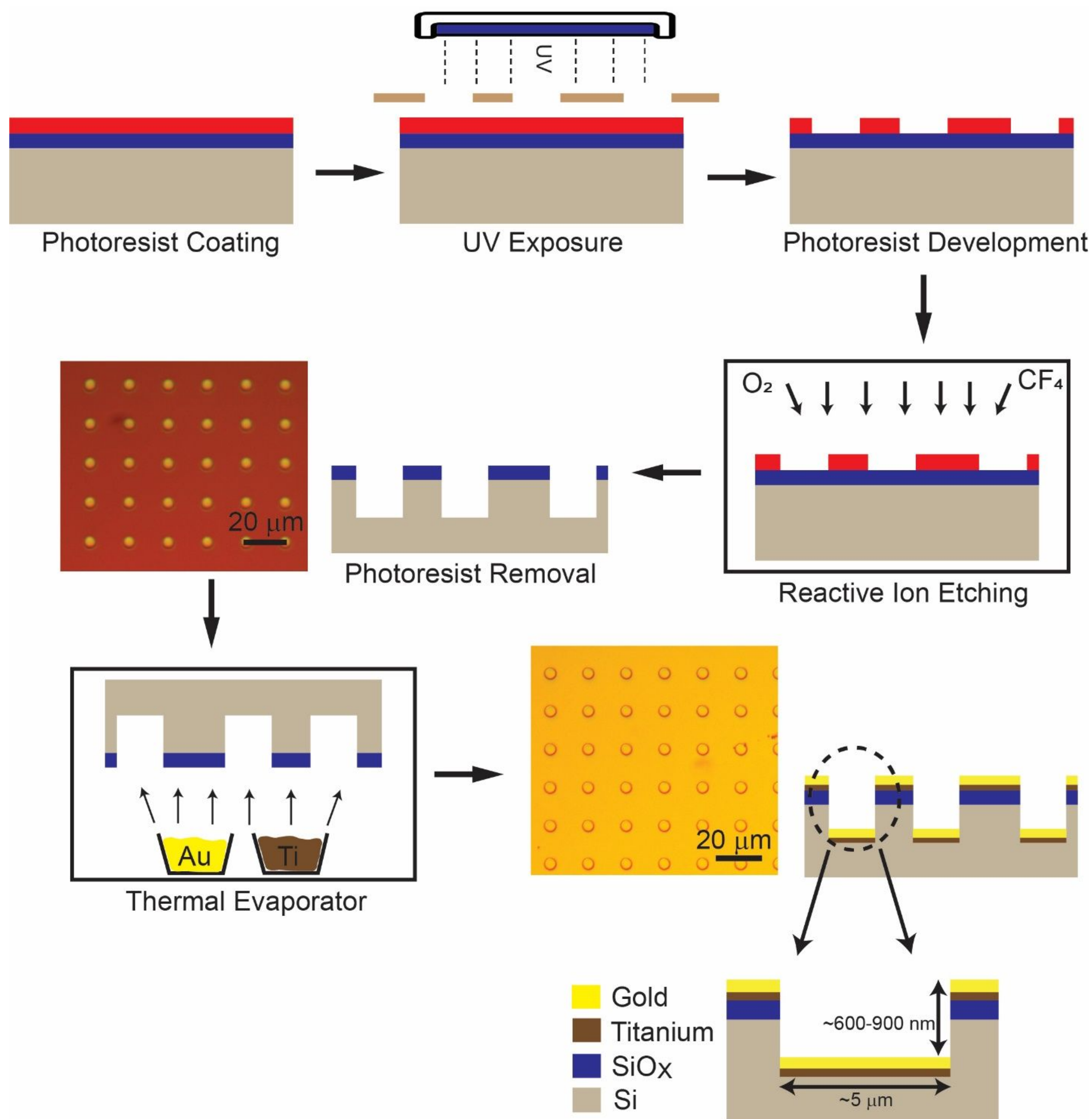

Figure S2. Microfabrication of the metal wells.

3. Graphite Substrate Fabrication

The preparation of the graphite wells starts with cleaning the SiO_x surface with acetone, IPA, and DI water. With the 'Scotch-Tape' method, freshly exfoliated flakes on tape are pressed against the oxide surface. The tape is peeled from the surface very slowly (~ 1 mm/min). The substrate is then spin-coated with S1818 at 2500 rpm and kept on the hot plate at 115 ^{o}C for 1 minute. The spin-coated chips are exposed to UV for 20 seconds with 8 mW power. Again, we use the same patterned mask during UV exposure to form the circular wells. Using RIE, we etch the wells to ~ 600-900 nm deep by deploying the same etching parameters as described above for the metal devices. Devices are then placed into the Remover 1165 bath at 110 ^{o}C over 12 hours and then exposed to O_2 plasma to remove any remaining photoresist (Fig. S3).

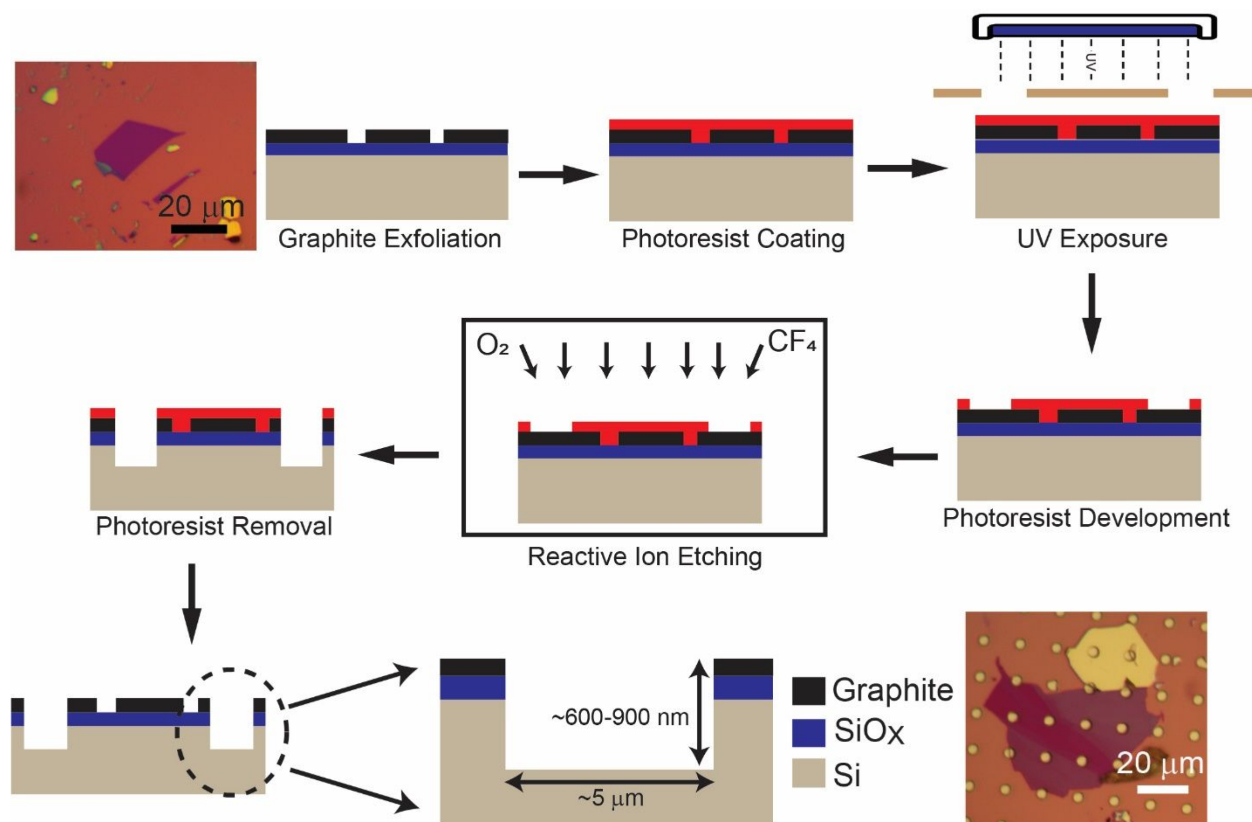

Figure S3. Microfabrication of the graphite wells.

4. Graphite Surface Treatment

Due to the O_2 plasma exposure for cleaning the graphite surface after photolithography, we performed Raman spectroscopy to determine if any surface chemistry changes took place. First, we carried out Raman spectroscopy over the freshly exfoliated flake (Fig. S4a) and again after photolithography and exposure to O_2 plasma during the final cleaning step (Fig. S4b). As can be seen in Figure S4b, a small D peak is introduced after O_2 plasma exposure indicative of the formation of defects[6] or graphite oxide formation[7] in the graphite lattice. However, the small size of the D peak suggests that the surface is not heavily oxidized.

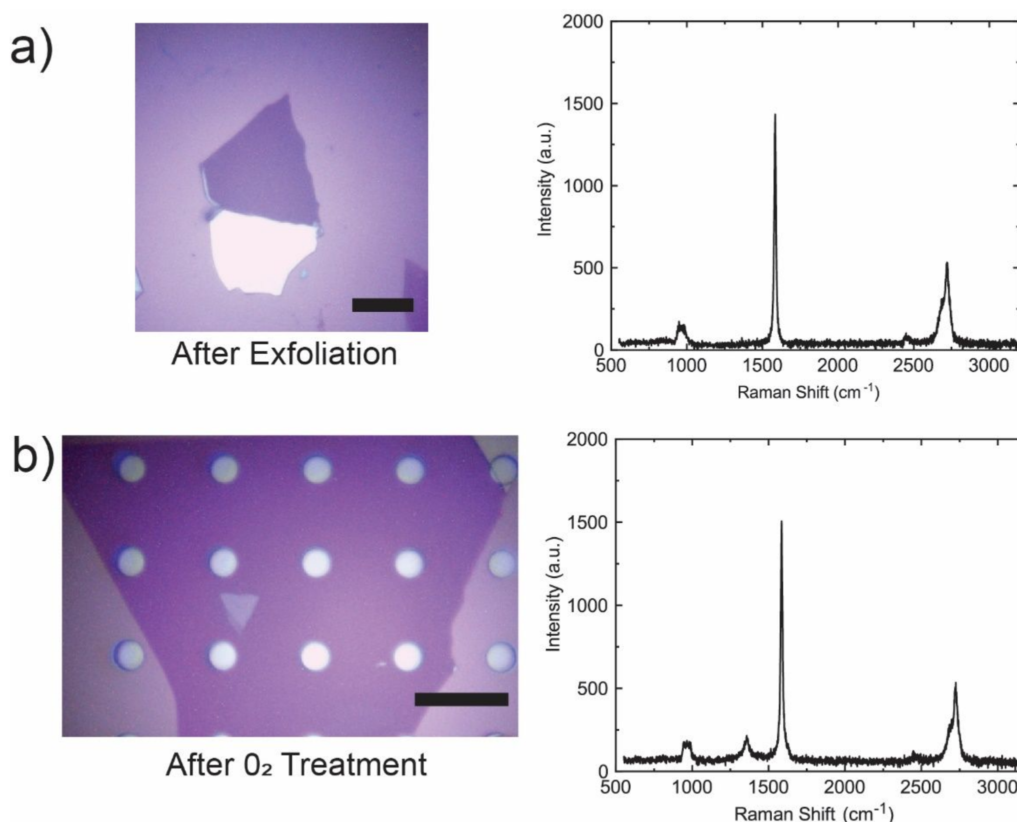

Figure S4. **a)** Optical image and Raman Spectrum of the freshly exfoliated graphite flake. Scale bar is 30 μm. **b)** Optical image and Raman spectroscopy of the etched FLG wells which exposed to O_2 plasma. The peak at 1400 cm^{-1} due to defects. Scale bars are 20 μm.

5. MoS_2 Transfer Procedure

The transfer of MoS_2 begins by spin coating the CVD-grown MoS_2 flakes with PMMA at 2500 rpm. We create a window on the thermal-release tape and it is stamped onto the PMMA-covered MoS_2 substrate. Utilizing the hydrophilic nature of the SiO_x/MoS_2 interface, we put this combination into water and let the water separate the MoS_2 flakes from the SiO_x substrate. This leaves us with a MoS_2/PMMA/Thermal-Release-Tape (MPT) combination.

Following the preparation of the MPT combination, metal and graphite substrates are both placed on a hot plate at 85 ^{o}C, and MPT is put onto the target substrate. For the graphite well, the transfer is carried out under the optical microscope with a custom-made apparatus that is used to keep the MPT still while approaching to surface. The Thermal-Release-Tape is peeled off from the surface easily with heat and the MoS_2/PMMA then sticks to the substrate. Before the annealing process, we put this device into a desiccator overnight (< 12 hr) to avoid any damage that trapped air inside the cavity may cause. The annealing process is carried out at 350 ^{o}C for 7 hours and under 20 sccm of Argon flow to help remove the PMMA from the surface (Fig. S5a). The transfer results are shown in the Fig. S5b (graphite) and Fig. S5c (gold).

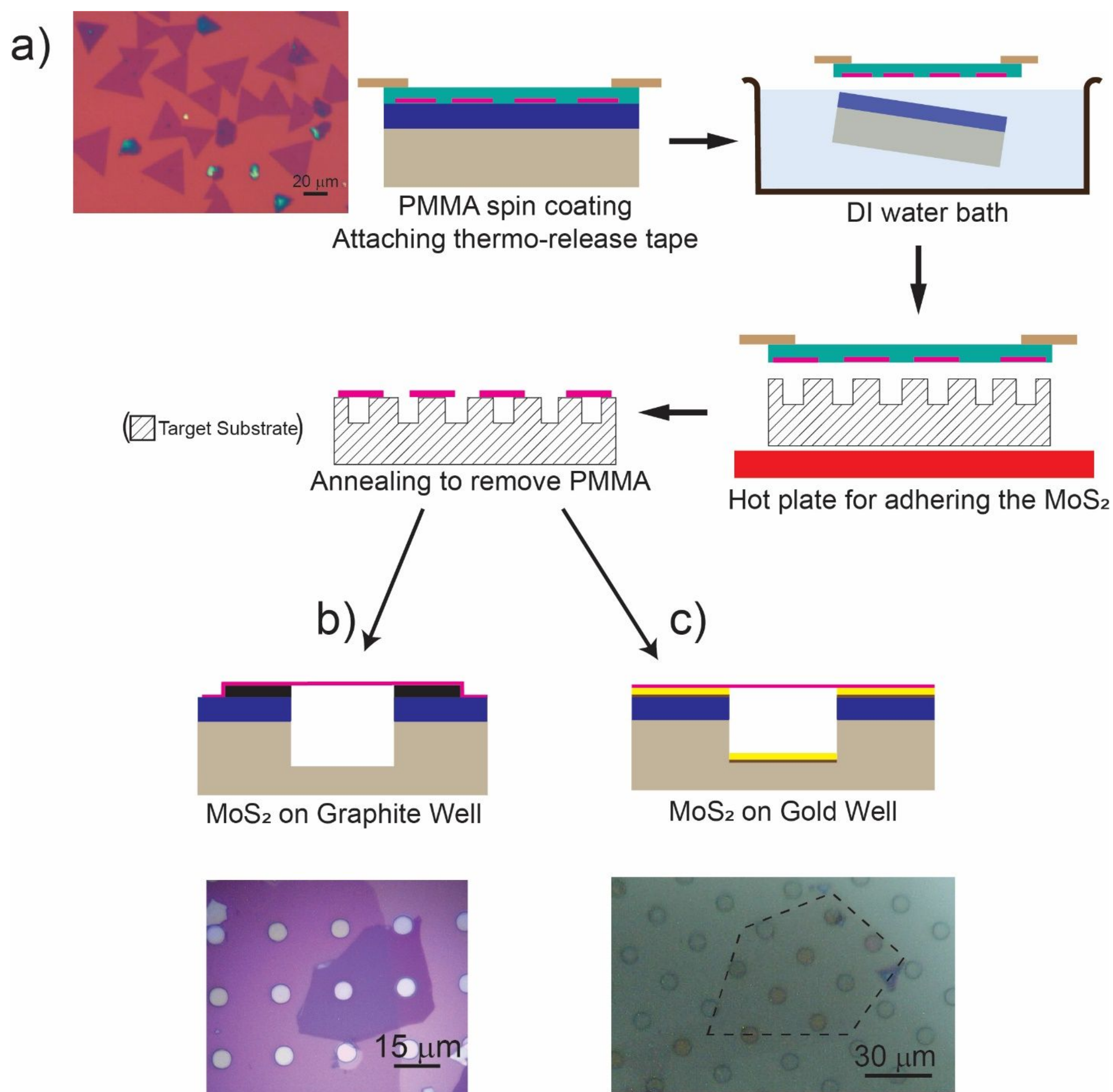

Figure S5. a) Schematic of monolayer MoS_2 flakes transfer over the target substrate. **b-c)** Optical image and schematic of the final result of the MoS_2 transfer over the graphite well and gold wells respectively. The dashed line in (c) shows the boundary of the MoS_2 flake.

6. Deriving the Expression for Pressure Difference and Deflection

Following the Hencky's solution for the deformation of a pressurized clamped axisymmetric membrane[8,9], we obtain the deflection profile as an infinite summation of even powers of normalized radius;

$$z(r) = a\left(\frac{\Delta p\, a}{Et}\right)^{1/3} \sum_{n=0}^{\infty} A_{2n}\left(1 - \left(\frac{r}{a}\right)^{2n+2}\right) \quad \text{S6.1}$$

with $A_0 = 1/B_0$, $A_2 = 1/2B_0^4$, $A_4 = 5/9B_0^7$, $A_6 = 55/72B_0^{10}$, $A_8 = 7/6B_0^{13}$, and so on. E is the bulk Young's modulus, t is the thickness of the membrane, and Δp is the pressure difference. The maximum height of the blister at the center can be found by $\delta \equiv z(r = 0)$ which yields:

$$\delta = a\left(\frac{\Delta p\, a}{Et}\right)^{1/3} \sum_{n=0}^{\infty} A_{2n} \quad \text{S6.2}$$

By setting $K(v) = 1/\left(\sum_{n=0}^{\infty} A_{2n}\right)^3$ and rearranging Eqn. S6.2, the final expression results in Eqn.1 of the main text.

One assumption of the constant-N blister test is the expansion of the membrane occurs isothermally, so we can model the change in the volume by ideal gas law which gives $p_0 V_0 = p_{int} (V_0 + V_b)$, where V_0 is the volume of the microcavity and $\Delta p = p_{int} - p_{ext}$. From Hencky's solution, the volume under the bulge is determined by the formula $V_b = C(v)\pi a^2 \delta$ where $C(v = 0.29) = 0.552$ since $v = 0.29$ [9,10] for MoS_2.

Below, we tabulate the constants *C, K* for a range of MoS_2 Poisson's ratio values commonly found in the literature (Table S1) and the corresponding calculated 2D Young's modulus and work of separation using these values. As can be seen, it does not influence the work of separation and has only a minor effect on the calculated elastic modulus.

	Poisson's Ratio (ν)	**K(ν)**	**C(ν)**	**E_{2D} (N/m)**	**Γ_{sep} (J/m^2)**
Device ID: R13	0.29	3.54	0.522	218.8	0.32
	0.25[11]	3.39	0.523	228.3	0.32

Table S1. Values for the constants C and K obtained with different Poisson's ratios and the E_{2D} and Γ_{sep} calculated using the corresponding constants.

7. Determining the Young's Modulus of MoS_2 over Graphite Devices

We examined 44 devices of MoS_2 over graphite substrates. In Fig. S6a, we plot $K(\nu)\, \delta^3/a^4$ vs Δp for 8 representative devices. In Fig. S6b, we show the full data set of the calculated E_{2D} values which were used to determine the work of separation(Fig. 4a in main text). Figure S6c shows an optical image of the graphite devices pinned to their initial radii, while the nearby membranes over the SiO_x wells show delamination at the same input pressure. Figure S6d-e are AFM images of those same devices showing that the MoS_2 over the graphite wells remains adhered while those on the SiO_x are delaminated for the same input pressure confirming the lower work of separation for MoS_2/SiO_x.

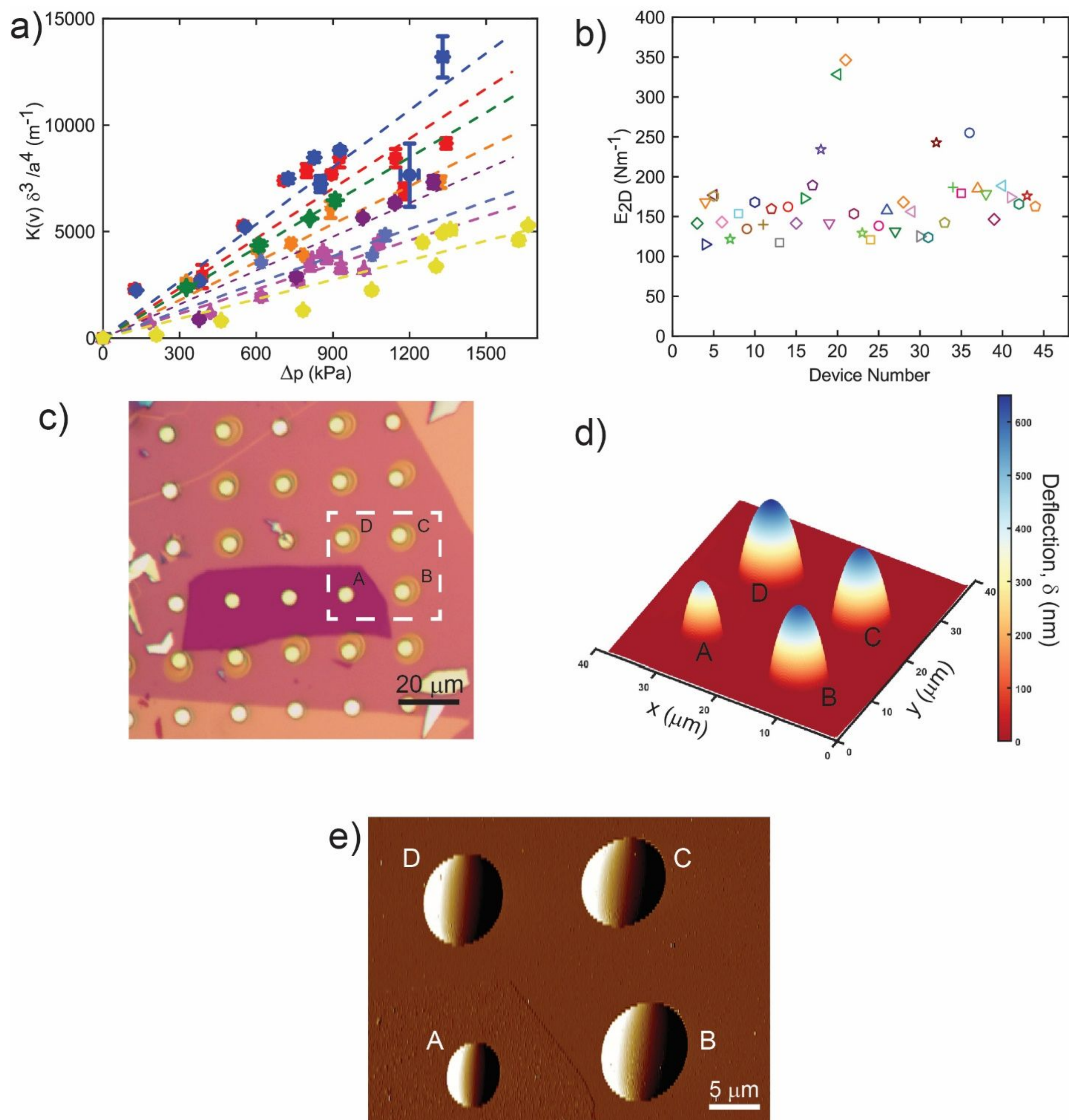

Figure S6. a) $K(v)\delta^3/a^4$ vs Δp for CVD-grown MoS_2 membranes. Dashed lines are the linear fits used to determine E_{2D} of each device. **b)** E_{2D} for each device. **c)** Optical image of MoS_2 over the graphite and SiO_x substrates (Device A is on the graphite and Devices B, C, and D are on the SiO_x). **d)** 3D AFM image of the devices labeled at (c). **e)** AFM Amplitude image of the devices labeled in (c).

8. Using Photoluminescence to Verify the Clamping Condition Assummed in Hencky's Model

MoS_2 shows changes in the optical band gap of ~ 100 meV/ % for biaxial strain[1,12]. Our membranes are subjected to biaxial strain near the center via a pressure difference $\Delta p = p_{int} - p_{ext}$. To validate the assumption in the Hencky model of a perfectly calmped circular membrane we used strain measurements determined by PL measurements and correlated them with strain measurements made by the AFM. A line scan of a series of PL measurements over the blister is shown in Fig. S7a. These are used to accurately determine the strain at the center of the membrane. In Figure S7b, we plot the PL response that corresponds to the points labeled with different colors indicating the different points (Fig. S7c, and d). In addition, we fit the Voigt function to each spectrum to follow the A exciton peak position[13]. We repeated the PL measurements for every new input pressure until delamination, and AFM scans accompany those measurements. We then correlated the AFM scans and PL measurements[8,9,14]. We use the stress-strain governing equations

$$\sigma_r - \upsilon\sigma_\theta = Et\varepsilon_r \quad \text{S8.1}$$

$$\sigma_\theta - \upsilon\sigma_r = Et\varepsilon_\theta \quad \text{S8.2}$$

where σ_r and σ_θ are radial and tangential membrane stresses respectively and ε_r and ε_θ are the radial and tangential strains. At the center of the membrane where $r = 0$, $\varepsilon_\theta = \varepsilon_r$ which is equivalent to perfect biaxial strain (ε_b). We can also write the equation for σ_r as an infinite series of even powers of radius r,

$$\sigma_r = \left(\frac{Et\Delta p^2\, a^2}{64}\right)^{1/3} \sum_{n=0}^{\infty} B_{2n}\left(\frac{r}{a}\right)^{2n} \quad \text{S8.3}$$

with $B_2 = -1/B_0^2$, $B_4 = -2/3B_0^5$, $B_6 = -13/18B_0^8$, $B_8 = -17/18B_0^{11}$, etc.

If we combine Eqn. S6.2 and S8.3 and Eqn. 1 from the main text, the final expression yields:

$$\varepsilon_b = \frac{B_0(v)(1-v)K(v)^{2/3}}{4}\left(\frac{\delta}{a}\right)^2 \quad \text{S8.4}$$

where B_o and K depend on Poisson's ratio and $K(v) = 1/\left(\sum_0^{\infty} A_{2n}\right)^3$. Using the Poisson's ratio for MoS_2 (v = 0.29), we obtain B_o = 1.72 and K = 3.54. We then substitute these values back into Eqn. S8.4 to obtain:

$$\varepsilon_b = 0.709\left(\frac{\delta}{a}\right)^2 \quad \text{S8.5}$$

From this expression, and knowing the maximum deflection and radius of the blister we calculate the biaxial strain at the center.

In Figure S7e, we plot the PL at the center of the blister vs. the strain calculated from the corresponding AFM scan for MoS_2 over the gold wells. The change in strain agrees with the theoretical change (~ 100 meV/%) validating the assumption of a perfectly clamped circular membrane assumed in the Hencky model. The laser is focused to a diffraction limited spot size of ~ 0.5 μm. The lateral spatial resolution is therefore ~ 0.5 μm. During the PL measurement, laser is kept focused over the scanned area.

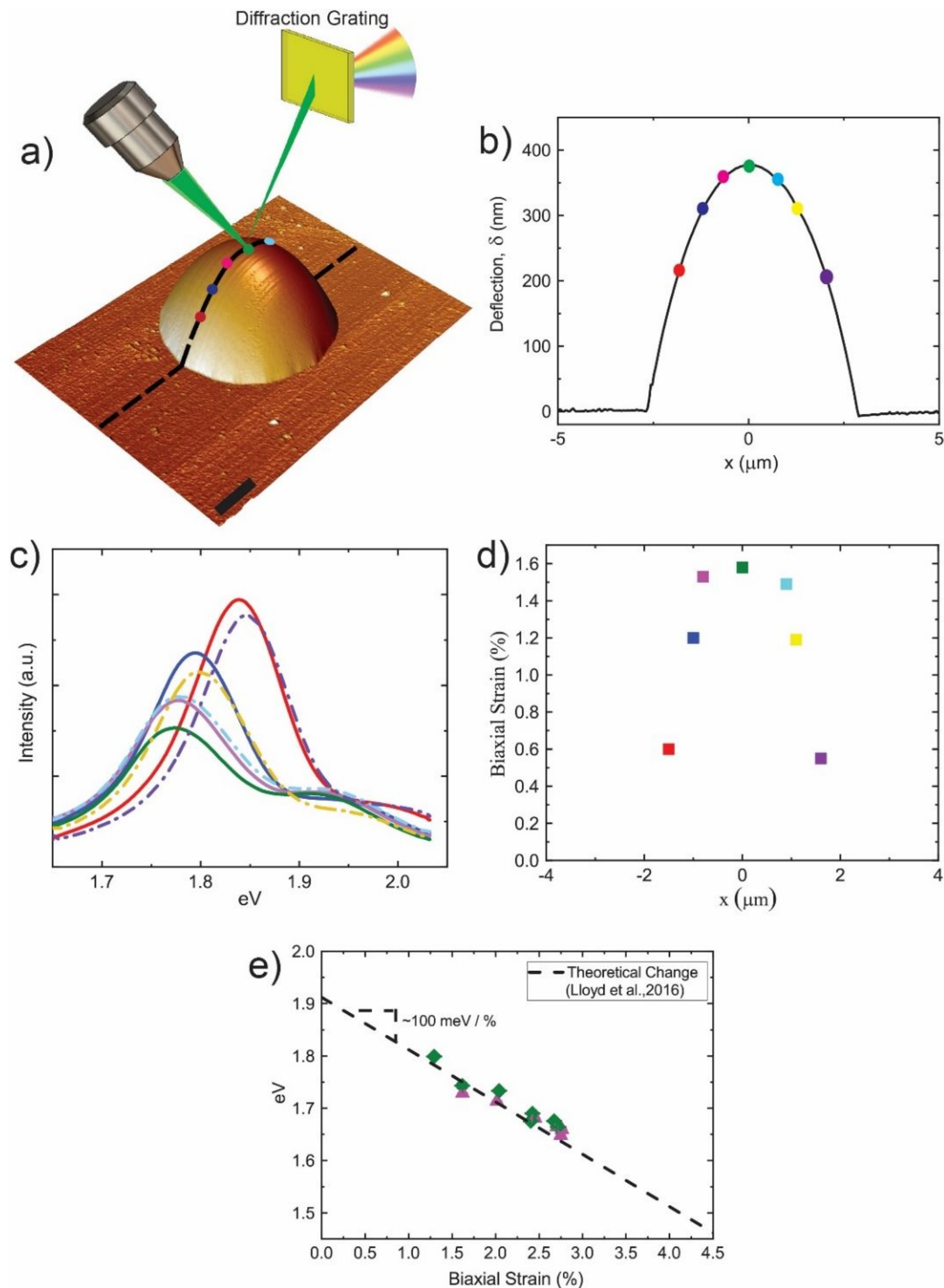

Figure S7. a) AFM image of the blister (height channel). The dashed line passes through the center of the blister where we conduct PL measurement over the points which are located along both sides of the blister. The scale bar is 2 μm. **b)** Positions of the PL measurement point on the cross-section of the device in (a). **c)** PL response of the data points labeled in (b) which we use the peak points in strain calculation. Solid lines correspond to points from the left edge of the blister to the center of the blister and dashed-dotted lines from the center to the right edge blister. **d)** Corresponding biaxial strain of the points in (c) by using their PL measurements. **e)** Calculation of the strain using the AFM results of each pressure change and matching them with corresponding PL data of MoS_2 on the gold wells. The dashed line is the theoretical change of the A exciton with respect to strain[1].

9. Strain Energy Derivation

In the paper, we closely follow the Wan et al. study[14,15] to calculate the contribution of the strain energy to our free energy model. First, we utilize equations described in the Hencky's solution. Aside from the governing equations mentioned before (Eqn. S6.1, S6.2, S8.1, and S8.2), we also use the following equations:

$$\sigma\theta = \frac{d}{dr}(r\sigma_r) \qquad \text{S9.1}$$

$$\varepsilon\theta = \frac{u}{r} \qquad \text{S9.2}$$

where u is radial displacement and r is radial polar coordinate. Wan et al. showed that the strain energy in the membrane is equal to the work done by the external load, i.e, gas pressure while keeping the blister radius a fixed.

$$F_{mem} = \int \Delta p(\delta)\, dV(\delta) \,\Big|_a = \frac{\Delta p\, V_b}{4} \qquad \text{S9.3}$$

Assuming $\xi = \frac{r}{a}$,we obtain the volume of the bulge as,

$$V_b = \int_0^a z(r) 2\pi r dr = a^2 \left(\frac{\Delta p\, a^4}{Et}\right)^{\frac{1}{3}} \int_0^1 z(\xi) 2\pi\xi d\xi \qquad \text{S9.4}$$

Using S6.1, we get:

$$F_{mem} = \frac{\Delta p\, a^2}{16} \left(\frac{\Delta p\, a^4}{Et}\right)^{1/3} \left(\frac{\pi}{8B_0} + \frac{\pi}{12B_0^4} + \frac{5\pi}{48B_0^7} + \frac{11\pi}{72B_0^{10}} + \frac{35\pi}{144B_0^{13}} + \frac{205\pi}{504B_0^{16}} + \frac{17051\pi}{24192B_0^{19}} + \frac{2864485\pi}{2286144B_0^{22}} + \frac{20772653\pi}{9144576B_0^{25}} + \frac{135239915\pi}{32332608B_0^{28}} + \frac{42367613873\pi}{5431878144B_0^{31}} + \dots\right) \qquad \text{S9.5}$$

It can be shown that Eqn. S9.5 is equal to the conventional expression for membrane strain energy[16] in Eqn. S9.6.

$$F_{mem} = \int_0^a \left(\frac{1}{2}\sigma_r\varepsilon_r + \frac{1}{2}\sigma_\theta\varepsilon_\theta\right) 2\pi r\, dr \qquad \text{S9.6}$$

We obtain ε_r and ε_θ by manipulating S8.1 and S8.2, respectively. After defining non-dimensional tangential stress component $\left(\sigma\theta = \frac{d}{dr}(r\sigma_r) \Rightarrow \sigma\theta = \frac{d}{d\xi}(\xi\sigma_r)\right)$, if we plug these back into Eqn. S9.6, we get:

$$F_{mem} = \pi a^2 \int_0^1 \left(\sigma_r^2 + \sigma_\theta^2 - 2\nu\sigma_r\sigma_\theta\right)\xi d\xi$$

$$= \pi a^2 \int_0^1 \left(2(1-\nu)\sigma_r^2 + 2(1-\nu)\xi\frac{d\sigma_r}{d\xi} + \xi^2\left(\frac{d\sigma_r}{d\xi}\right)^2\right)\xi d\xi \qquad \text{S9.7}$$

$$= \pi a^2 \int_0^1 \left(\frac{d}{d\xi}\left((1-\nu)\xi^2\sigma_r^2\right) + \xi^3\left(\frac{d\sigma_r}{d\xi}\right)^2\right) d\xi$$

The clamped boundary condition gives us the following relation:

$$u(\xi = 1) = 0 \Rightarrow \sigma_\theta(\xi = 1) - \nu\sigma_r(\xi = 1) = 0 \Rightarrow$$

$$(1-\nu)\sigma_r(\xi = 1)^2 = -\xi\,\sigma_r(\xi = 1)\left(\frac{d\sigma_r}{d\xi}(\xi = 1)\right) \qquad \text{S9.8}$$

After integrating the first term in the integrand, the final formula yields:

$$F_{mem} = \pi a^2 \left(\int_0^1 \xi^3 \left(\frac{d\sigma_r}{d\xi}\right)^2\right) d\xi - \pi\left(\sigma_r(\xi = 1)\frac{d\sigma_r(\xi = 1)}{d\xi}\right) \qquad \text{S9.9}$$

Computing the Eqn. S9.9 using the series expressions for σ_r (Eqn. S8.3) gives us:

$$F_{mem} = \frac{\Delta p\, a^2}{16}\left(\frac{\Delta p\, a^4}{Et}\right)^{\frac{1}{3}}\left(\frac{\pi}{8B_0} + \frac{\pi}{12B_0^4} + \frac{5\pi}{48B_0^7} + \frac{11\pi}{72B_0^{10}} + \frac{35\pi}{144B_0^{13}} + \frac{205\pi}{504B_0^{16}} + \frac{17051\pi}{24192B_0^{19}} + \frac{2864485\pi}{2286144B_0^{2}} + \frac{20772653\pi}{9144576B_0^{25}} + \frac{135239915\pi}{32332608B_0^{28}} + \frac{42367613873\pi}{5431878144B_0^{31}} + \frac{1120150157\pi}{76212576B_0^{34}} + \frac{35059666851}{12547638512} + \dots\right) \quad \text{S9.10}$$

As can be seen, the series in Eqns. S9.5 and S9.10 are identical.

10. Relamination of MoS_2 over the Metal and Graphite Wells

In Figure S8, the complete deflation data for 9 devices of MoS_2 over gold substrates are shown. We obtain a mean value of $\Gamma_{adh} = 0.017 \pm 0.005$ J/m^2. Figure S8b is the optical image of the delaminated device, and Figure S8c-h are AFM images showing relamination. The adhesion hysteresis observed is reminiscent of AFM based nanoindentation studies. In these studies the hysteresis has been attributed to moisture[17,18], viscoelasticity[19], plasticity[20], and surface instabilities[21,22]. Similar mechanisms as these may be at work in our case as well. The

measurements of the deflection and radius are performed along the cross-sections shown in Fig. S8c and only the mean values of these measurements are shown in Fig. S8a for clarity.

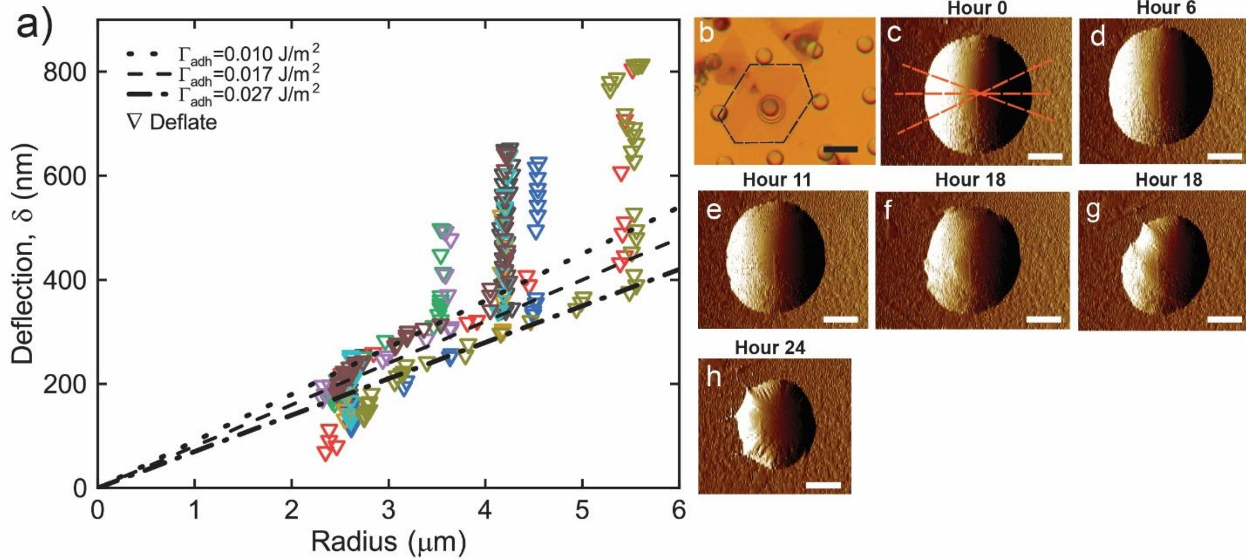

Figure S8. a) Complete data of deflation for 9 devices. Each color represents a different device. The dashed line is the mean value of all samples (Γ_{adh} = 0.017 ± 0.005 J/m^2 (Dashed line). **b)** Optical image of the delaminated devices. The scale bar is 10 μm. **c-d)** AFM images(amplitude channel) of the device in (b). Elapsed times are put on top of each photo. The dashed lines in (c) are the cross-sections that are used for deflection and radius change. The scale bars are 3 μm.

In Figure S9, we plot the deflation data sets for the MoS_2 on the FLG substrates. We performed the measurements on 9 different devices and found Γ_{adh} = 0.057 ± 0.008 J/m^2 (dashed line). Fig. S9b is the optical image of the devices and its deflation behavior is shown in Fig. S9c-k with each labeled with the elapsed time of the measurement.

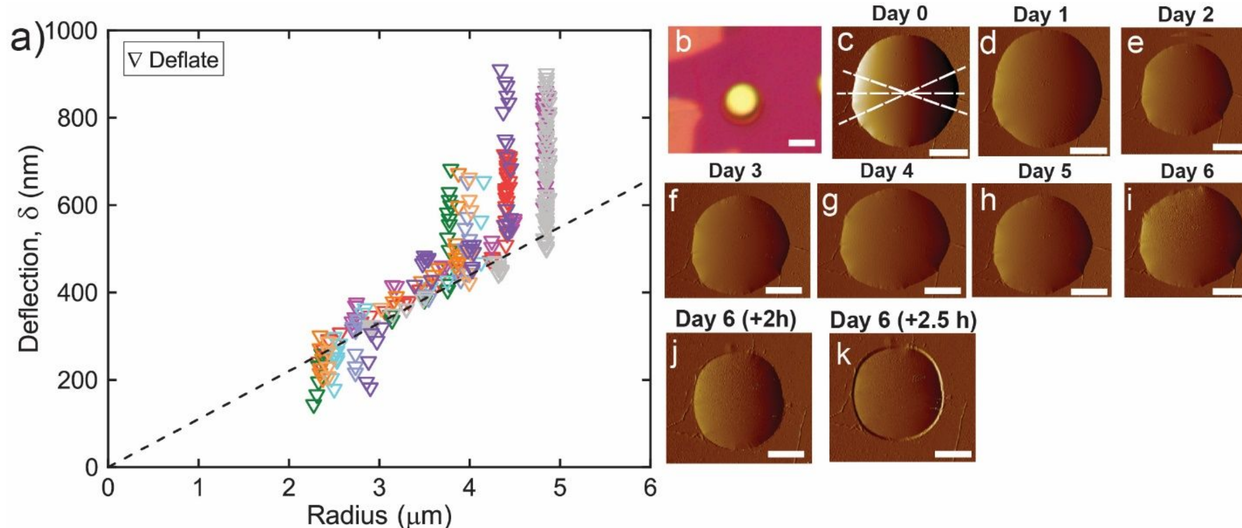

Figure S9. a) Complete deflation data for 9 graphite devices. Each color represents a different device. The dashed line is the mean value of all samples shown in Fig. 4d ($\Gamma_{rel} = 0.057 \pm 0.008$ J/m^2). **b)** Optical image of a delaminated device. The scale bar is 5 μm. **c-k)** AFM images (amplitude channel) of the device in (b). Elapsed times are included. The dashed lines in (c) are the cross-sections that are used for the measurement of deflection and radius. The scale bars are 3μm.

In Figure S10, we examine the MoS_2 over Si wells and in Fig. S10a we plot $K(v)\delta^3/a^4$ vs Δp. A linear fit to the data is used to determine E_{2D} for each device. These calculated E_{2D} values are used in the separation and adhesion energy calculations of these membrane from the Si wells. In Figure S10b, we show the values of E_{2D} determined from the fit in Fig. S10a. Figure S10c is the deflation data for the MoS_2 on the Si substrates. We performed the measurements on 5 different devices. We found a work of adhesion $\Gamma_{adh} = 0.03 \pm 0.0018$ J/m^2 (dashed line).

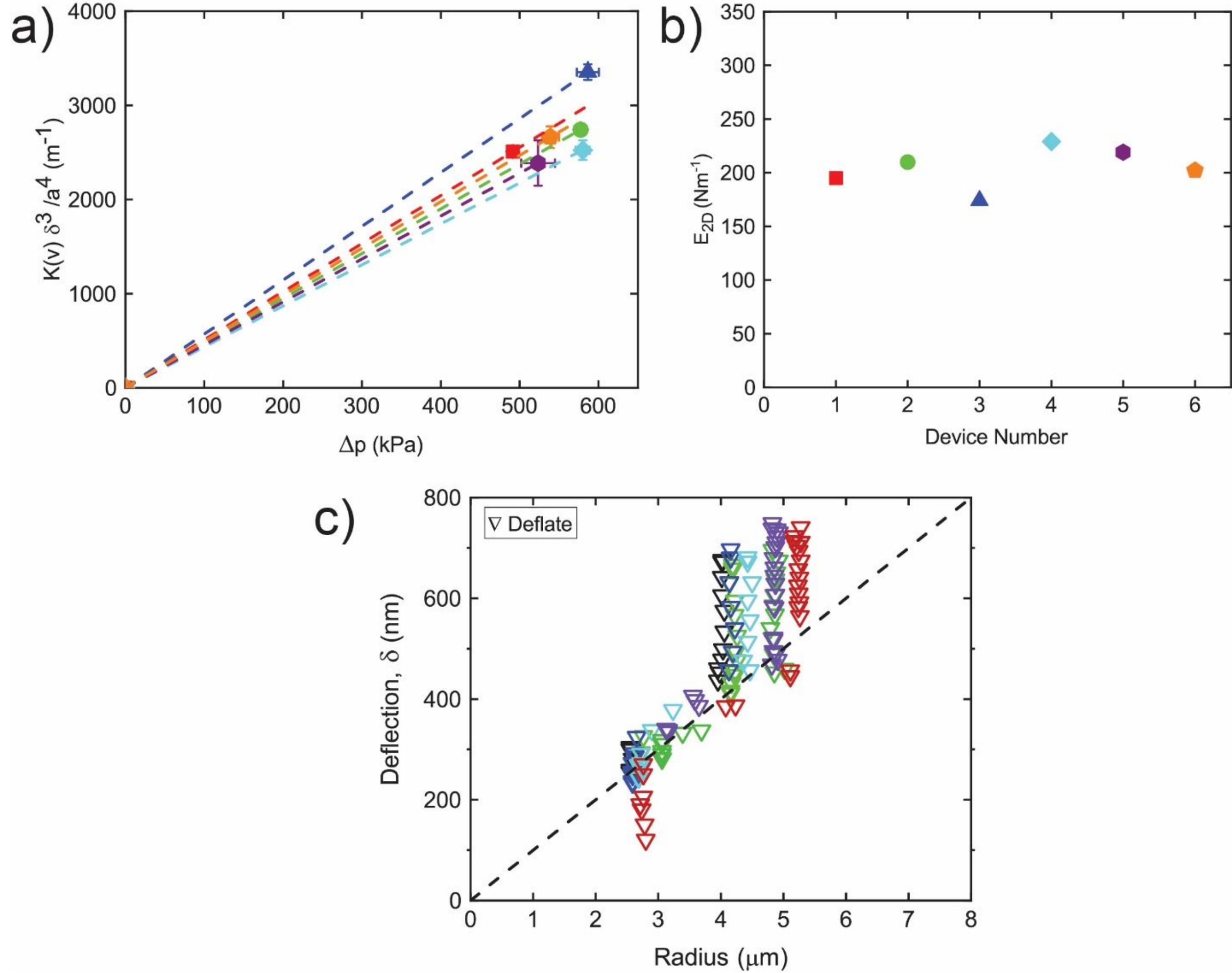

Figure S10. Data for Si substrates. **a)** $K(\nu)\delta^3/a^4$ vs Δp for CVD-grown MoS_2 membranes. Dashed lines are the linear fits that are used to calculate E_{2D} of each device. Symbols are color-coded. **b)** E_{2D} for each device **c)** Maximum deflection, δ, and radius during the deflation. The dashed line is the mean value of all samples.

In Figure S11 we examine the MoS_2 over SiO_x wells and in Fig. S11a we plot $K(\nu)\delta^3/a^4$ vs Δp. A linear fit to the data is used to determine E_{2D} for each device. In Figure S11b, we show the values of E_{2D} determined from the fit in Fig. S11a. These calculated E_{2D} values are used in the separation and adhesion energy calculations of these membrane from the SiO_x wells.

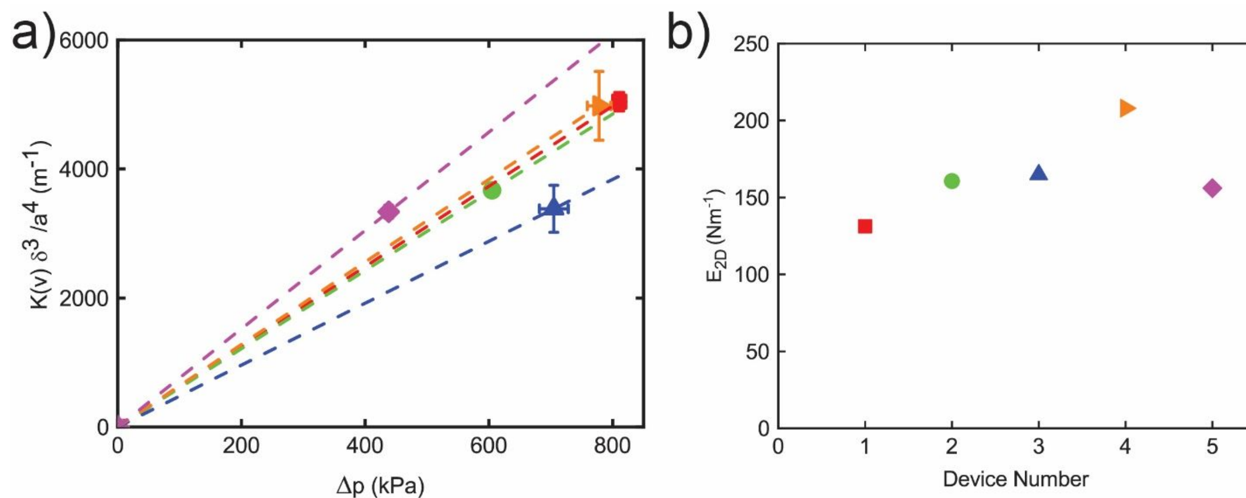

Figure S11. Data for SiO_x substrates. **a)** $K(v)\delta^3/a^4$ vs Δp for CVD-grown MoS_2 membranes. Dashed lines are the linear fits that are used to calculate E_{2D} of each device. Symbols are color-coded. **b)** E_{2D} for each device.

In Figures S12 through S14, we examine the MoS_2 over Titanium, Chromium, and Germanium wells. In each figure, we plot $K(v)\delta^3/a^4$ vs Δp. A linear fit to the data is used to determine E_{2D} for each device. Later, we show the values of E_{2D} determined from the fits which are used in the separation and adhesion energy calculations for each substrate. The average work of adhesion can be found in the caption of the figures for each material.

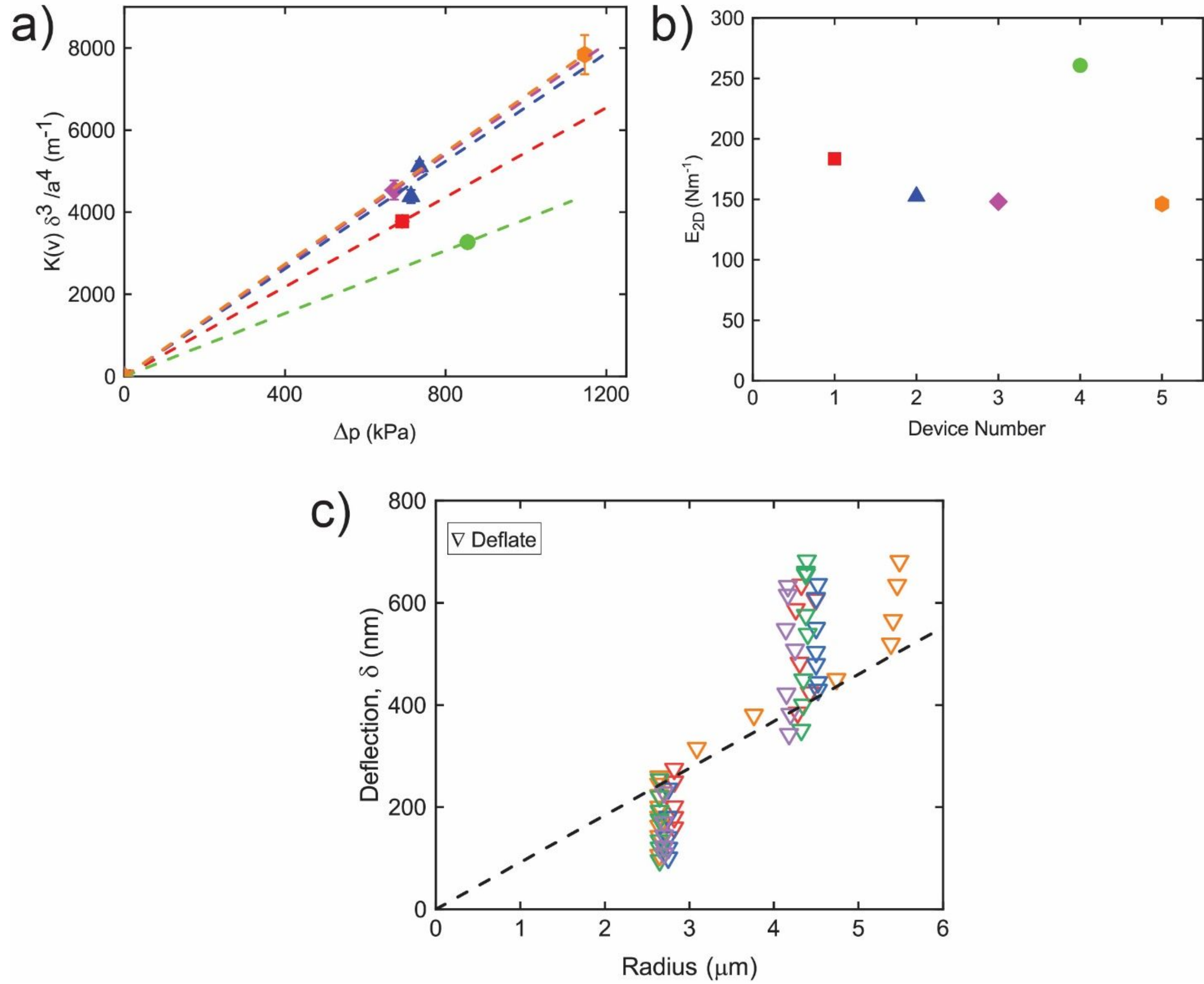

Figure S12. Data for Titanium substrates. **a)** $K(v)\delta^3/a^4$ vs Δp for CVD-grown MoS_2 membranes. Dashed lines are the linear fits that are used to calculate E_{2D} of each device. Symbols are color-coded. **b)** E_{2D} for each device. **c)** δ vs radius during deflation. The dashed line is the mean value of all samples. $\Gamma_{adh} = 0.03 \pm 0.004$ J/m^2

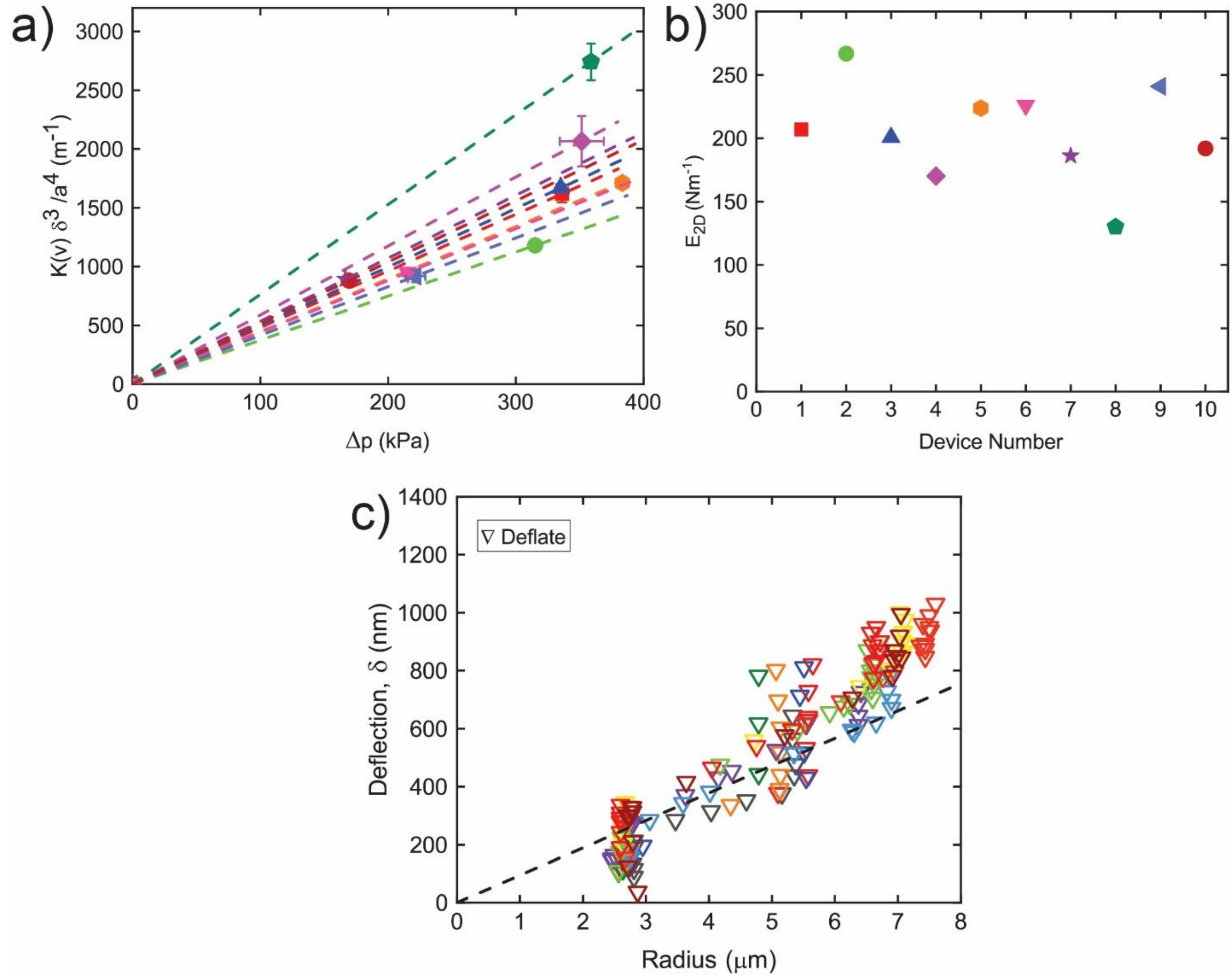

Figure S13. Data for Chromium substrates. **a)** $K(v)\delta^3/a^4$ vs Δp for CVD-grown MoS_2 membranes. Dashed lines are the linear fits that are used to calculate E_{2D} of each device. Symbols are color-coded. **b)** E_{2D} for each device. **c)** δ and radius during deflation. The dashed line is the mean value of all samples. $\Gamma_{adh} = 0.036 \pm 0.018$ J/m^2.

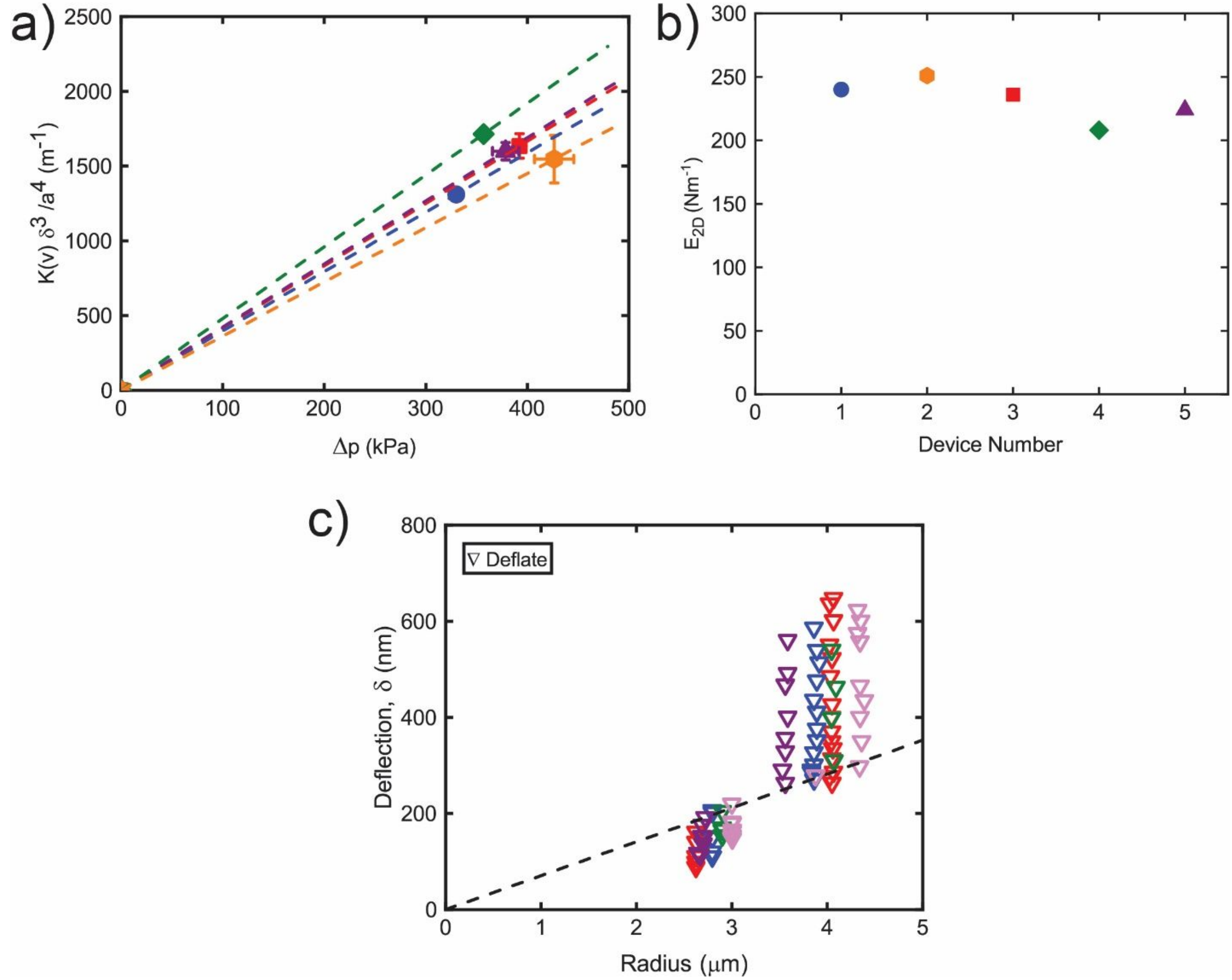

Figure S14. Data for Germanium substrates. **a)** $K(v)\delta^3/a^4$ against Δp for CVD-grown MoS_2 membranes. Dashed lines are the linear fits that are used to calculate E_{2D} of each device. Symbols are color-coded. **b)** E_{2D} for each device. **c)** δ and radius during deflation. The dashed line is the mean value of all samples. $\Gamma_{adh} = 0.012 \pm 0.002$ J/m^2.

11. Roughness Measurements over the Substrates

To determine the influence of surface roughness on the work of separation , we measured the surface roughness of our substrates using an AFM. First, we performed the AFM scans after the fabrication of the substrate. Following the MoS_2 transfers over the wells, we performed another AFM scan over the MoS_2 covered areas. AFM scans are conducted in a 250 nm x 500 nm area in

tapping mode. Then, we analyzed 100 nm x 100 nm sub-areas within the scans to determine the root-mean-square (rms) values of the roughness using the NanoScope Analysis 2.0 program. The same scan sizes, and parameters are used for all of the scans.

In the following graphs, we show the AFM height images and the repsentative line cut through the scan area to demonstrate the surface roughness for each substrate used in our experiment.

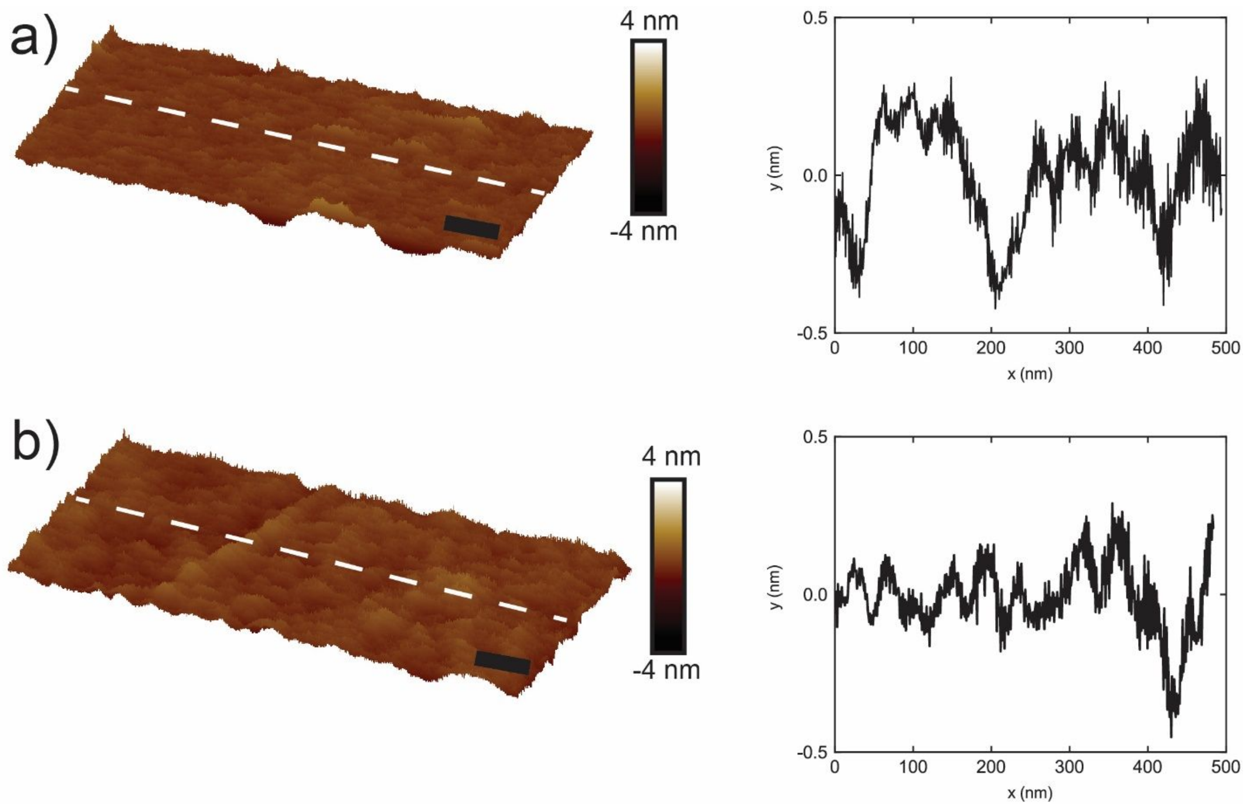

Figure S15. Si substrate. **a)** AFM scan over bare substrate fabrication of wells. **b)** Scan over MoS_2 covered area after annealing. Scale bars are 50 nm.

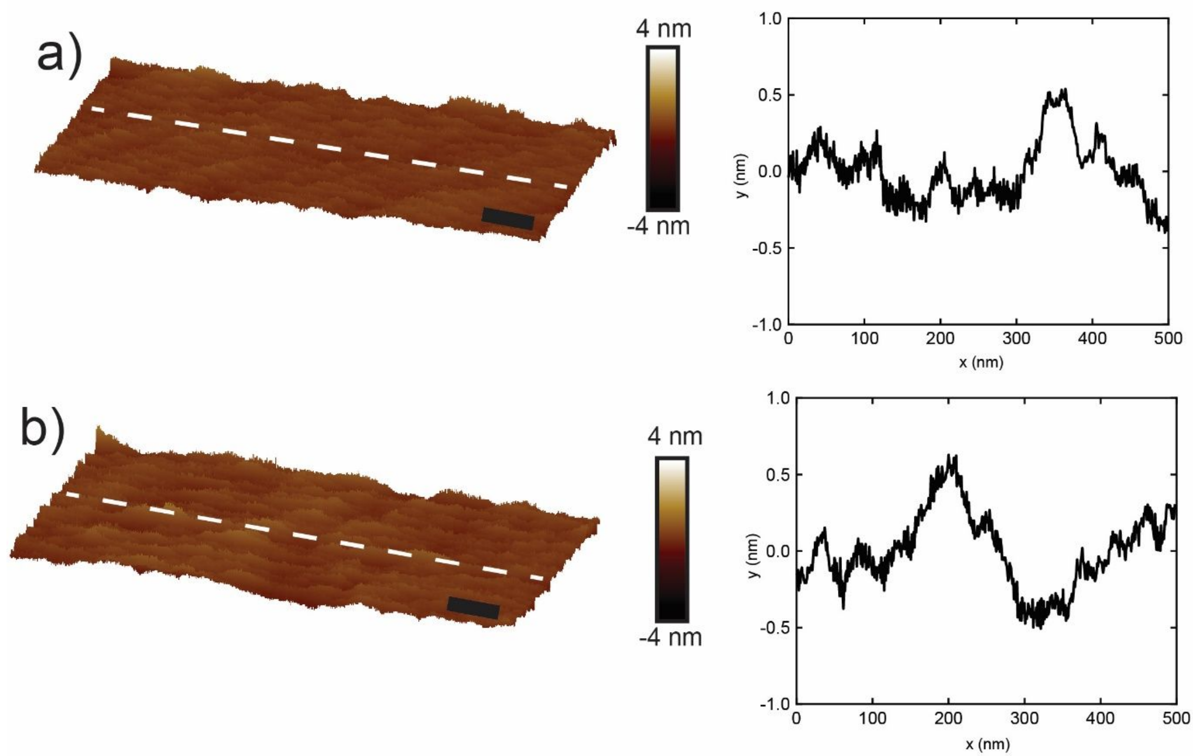

Figure S16. SiO_x substrate. **a)** AFM scan over bare substrate after fabrication of wells. **b)** Scan over MoS_2 covered area after annealing. Scale bars are 50 nm.

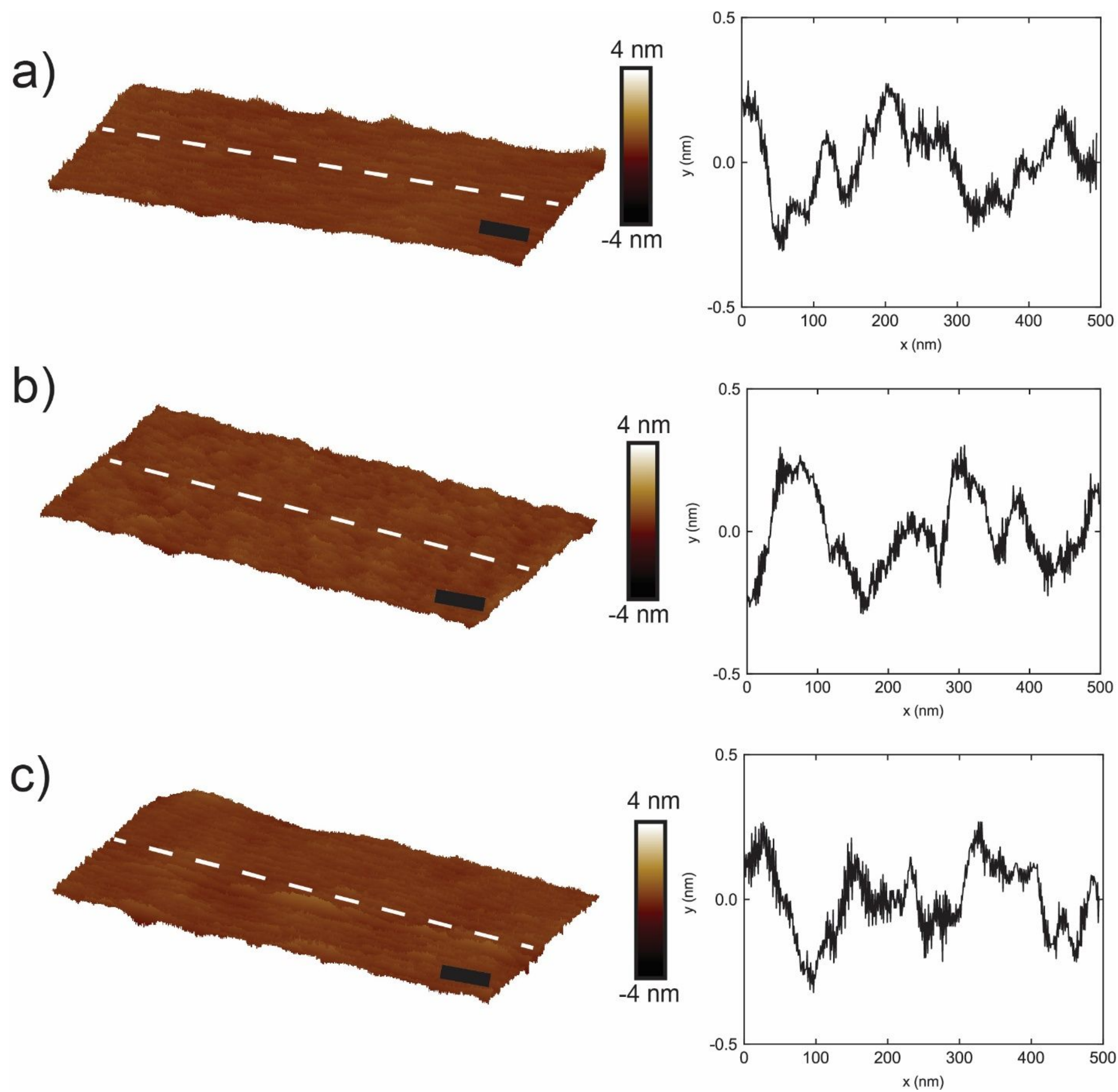

Figure S17. Graphite substrate. **a)** AFM scan after fabrication of wells. **b)** Scan over bare substrate after annealing. **c)** Scan over MoS_2 covered area after annealing. Scale bars are 50 nm.

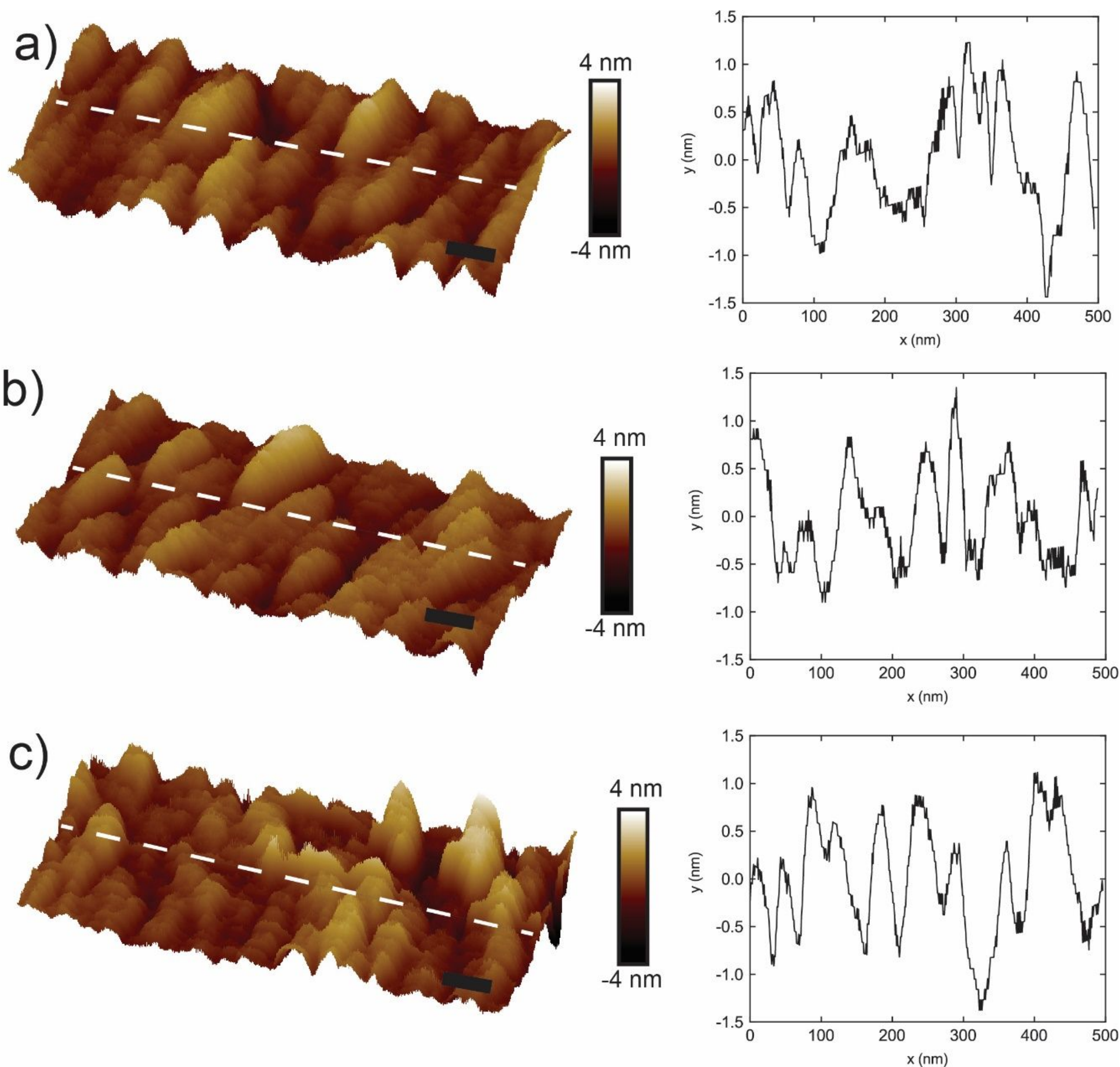

Figure S18. Gold substrate. **a)** AFM scan after fabrication of wells. **b)** Scan over bare substrate after annealing. **c)** Scan over MoS_2 covered area after annealing. Scale bars are 50 nm.

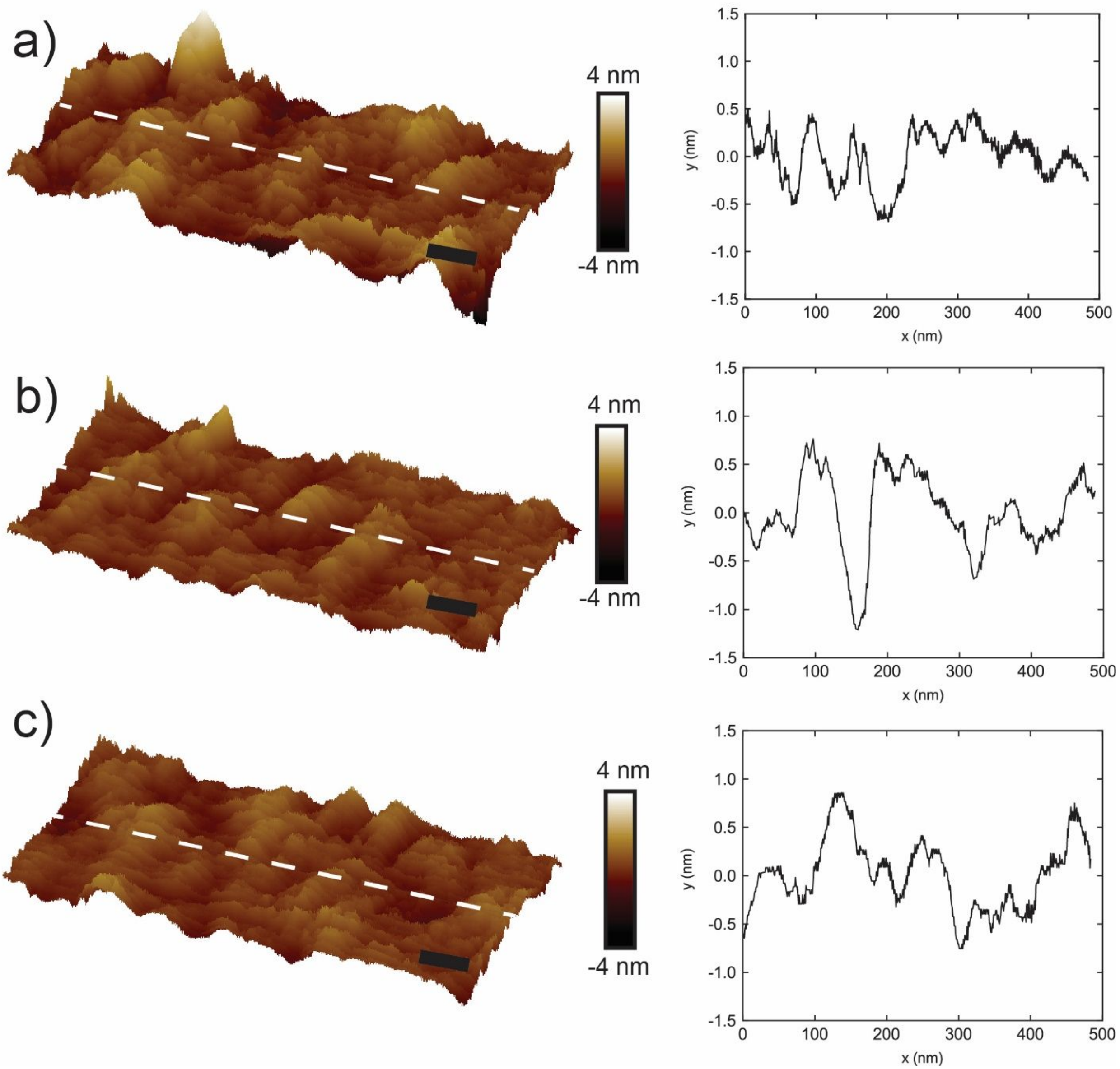

Figure S19. Titanium substrate. **a)** AFM scan after fabrication of wells **b)** Scan over bare substrate after annealing. **c)** Scan over MoS_2 covered area after annealing. Scale bars are 50 nm.

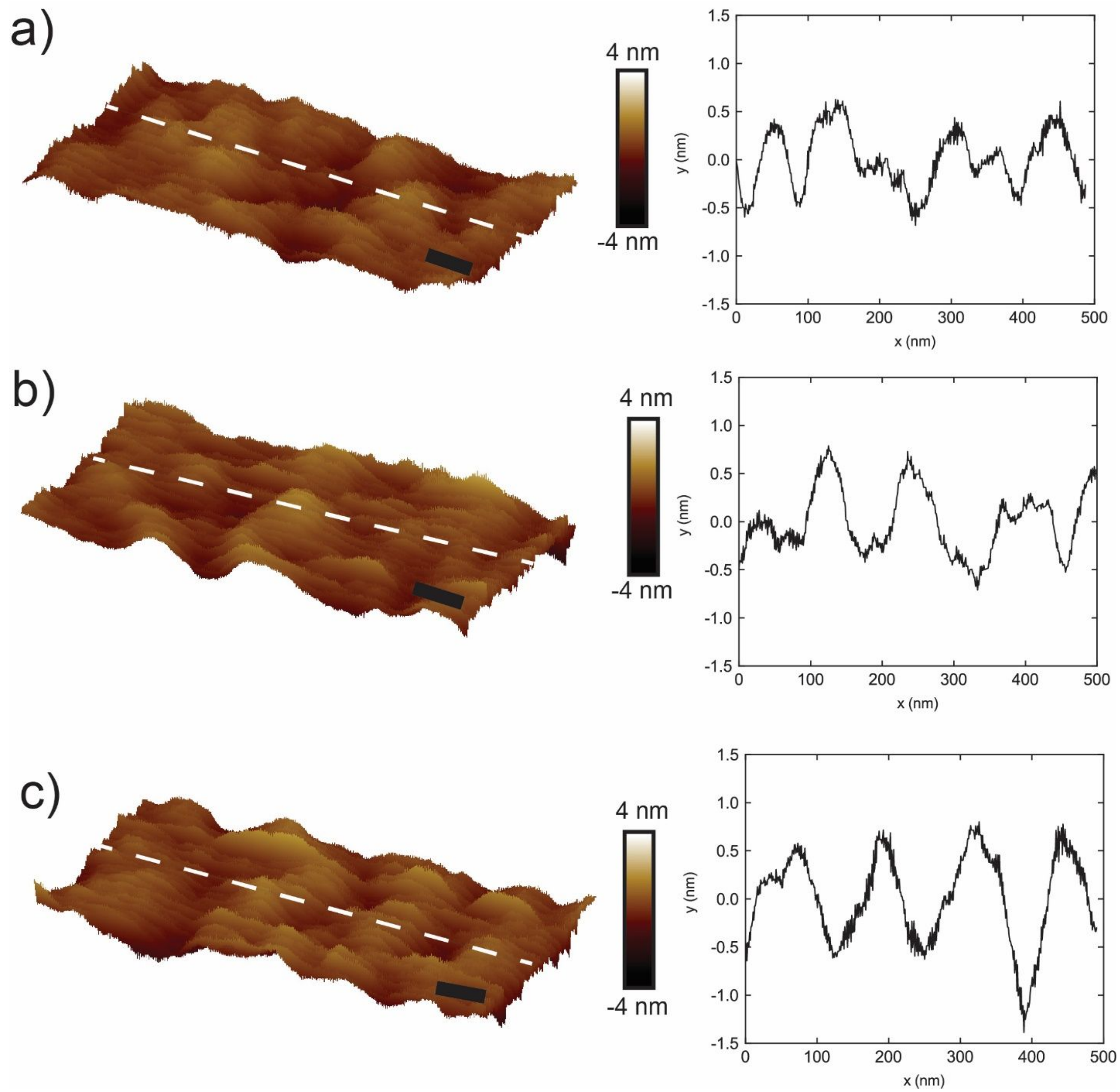

Figure S20. Chromium substrate. **a)** AFM scan after fabrication of wells **b)** Scan over bare substrate after annealing. **c)** Scan over MoS_2 covered area after annealing. Scale bars are 50 nm.

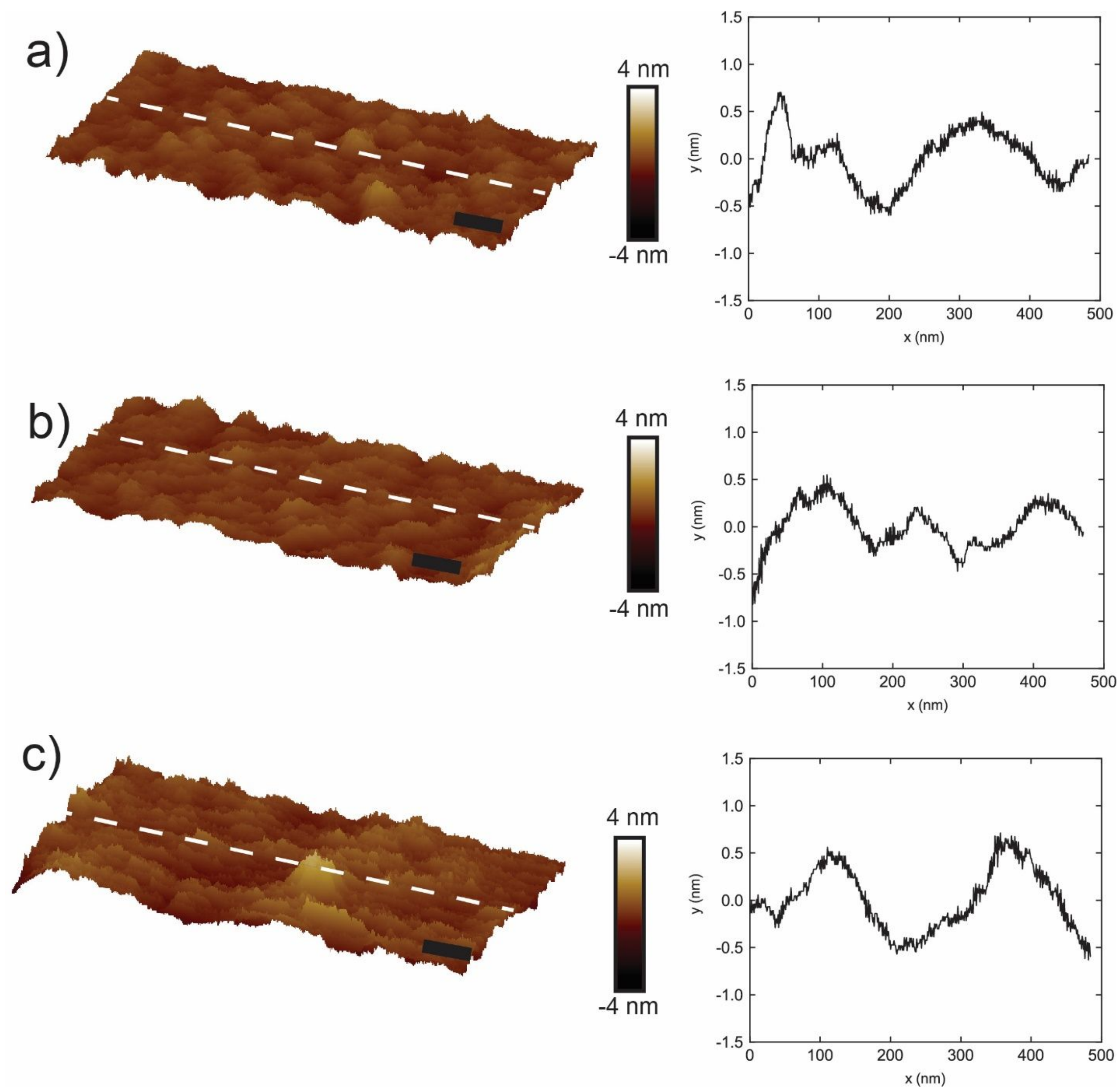

Figure S21. Germanium substrate. **a)** AFM scan after fabrication of wells **b)** Scan over bare substrate after annealing. **c)** Scan over MoS_2 covered area after annealing. Scale bars are 50 nm.

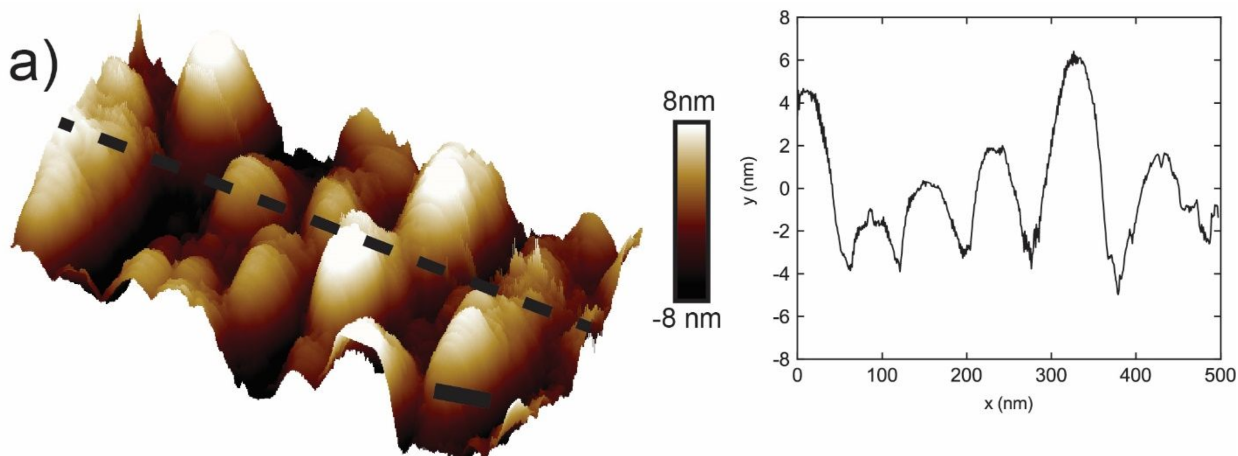

Figure S22. Aluminium substrate. **a)** AFM scan after fabrication of wells. Scale bar is 50 nm.

In Table S2, the results of the AFM scans over the substrates are tabulated.

Substrate Material	Roughness Measurements (Averaged RMS Values)			Work of Separation (Jm^{-2})	Work of Adhesion (Jm^{-2})
	Over the Bare Substrate Before Annealing (nm)	Over the Bare Substrate After Annealing (nm)	Over the MoS_2 Flake (nm)		
Si	0.15±0.02	N/A	0.21±0.04	0.20±0.03	0.03±0.018
SiO_x	0.18±0.01	N/A	0.20±0.02	0.22±0.01	N/A
Graphite	0.21±0.04	0.27±0.03	0.26±0.01	0.39±0.1	0.05±0.01
Gold	0.7 ±0.08	0.57±0.04	0.6 ±0.02	0.28±0.04	0.017±0.005
Chromium	0.48±0.02	0.45±0.03	0.5±0.04	0.11±0.05	0.036±0.018
Germanium	0.32±0.04	0.32±0.01	0.33±0.02	0.12±0.04	0.01±0.002
Titanium	0.4±0.08	0.35±0.02	0.36±0.1	0.14±0.03	0.033±0.004
Aluminium	3.8±0.8	N/A	N/A	N/A	N/A

Table S2. Summary of roughness measurements.

12. Transfer of MoS_2 Membranes over Various Substrates

Videos showing the transfer of the MoS_2 onto the Silicon Oxide (video 1), Chromium (video 2), Titanium (video 3), and Aluminum (video 4) surfaces. In video 4, we attempted to transfer MoS_2 over the aluminum coated surface but were unsuccessful. Aluminum had the highest surface roughness and MoS_2 was unable to be transferred.

References

(1) Lloyd, D.; Liu, X.; Christopher, J. W.; Cantley, L.; Wadehra, A.; Kim, B. L.; Goldberg, B. B.; Swan, A. K.; Bunch, J. S. Band Gap Engineering with Ultralarge Biaxial Strains in Suspended Monolayer MoS2. *Nano Lett.* **2016**, *16* (9), 5836–5841. https://doi.org/10.1021/acs.nanolett.6b02615.

(2) Wu, S.; Huang, C.; Aivazian, G.; Ross, J. S.; Cobden, D. H.; Xu, X. Vapor-Solid Growth of High Optical Quality MoS2 Monolayers with near-Unity Valley Polarization. *ACS Nano* **2013**, *7* (3), 2768–2772. https://doi.org/10.1021/nn4002038.

(3) Li, H.; Wu, J.; Huang, X.; Lu, G.; Yang, J.; Lu, X.; Xiong, Q.; Zhang, H. Rapid and Reliable Thickness Identification of Two-Dimensional Nanosheets Using Optical Microscopy. *ACS Nano* **2013**, *7* (11), 10344–10353. https://doi.org/10.1021/NN4047474.

(4) Li, F.; Huang, T. De; Lan, Y. W.; Lu, T. H.; Shen, T.; Simbulan, K. B.; Qi, J. Anomalous Lattice Vibrations of CVD-Grown Monolayer MoS2 Probed Using Linear Polarized Excitation Light. *Nanoscale* **2019**, *11* (29), 13725–13730. https://doi.org/10.1039/C9NR03203G.

(5) Mak, K. F.; He, K.; Lee, C.; Lee, G. H.; Hone, J.; Heinz, T. F.; Shan, J. Tightly Bound Trions in Monolayer MoS2. *Nat. Mater. 2012 123* **2012**, *12* (3), 207–211. https://doi.org/10.1038/nmat3505.

(6) Kaniyoor, A.; Ramaprabhu, S. A Raman Spectroscopic Investigation of Graphite Oxide Derived Graphene. *AIP Adv.* **2012**, *2* (3), 032183. https://doi.org/10.1063/1.4756995.

(7) Perumbilavil, S.; Sankar, P.; Priya Rose, T.; Philip, R. White Light Z-Scan Measurements of Ultrafast Optical Nonlinearity in Reduced Graphene Oxide Nanosheets in the 700 Nm Region. *Appl. Phys. Lett.* **2015**, *107* (5), 051104. https://doi.org/10.1063/1.4928124.

(8) Fichter, W. B. Some Solutions for the Large Deflections of Uniformly Loaded Circular Membranes. *NASA Tech. Pap.* **1997**, *3658*, 1–24.

(9) Lloyd, D.; Liu, X.; Boddeti, N.; Cantley, L.; Long, R.; Dunn, M. L.; Bunch, J. S. Adhesion, Stiffness, and Instability in Atomically Thin MoS2 Bubbles. *Nano Lett.* **2017**, *17* (9), 5329–5334. https://doi.org/10.1021/acs.nanolett.7b01735.

(10) Cooper, R. C.; Lee, C.; Marianetti, C. A.; Wei, X.; Hone, J.; Kysar, J. W. Nonlinear Elastic Behavior of Two-Dimensional Molybdenum Disulfide. *Phys. Rev. B - Condens. Matter Mater. Phys.* **2013**, *87* (3), 035423. https://doi.org/10.1103/PhysRevB.87.035423.

(11) Kang, J.; Sahin, H.; Peeters, F. M. Mechanical Properties of Monolayer Sulphides: A Comparative Study between MoS2, HfS2 and TiS3. *Phys. Chem. Chem. Phys.* **2015**, *17* (41), 27742–27749. https://doi.org/10.1039/C5CP04576B.

(12) Yang, R.; Lee, J.; Ghosh, S.; Tang, H.; Sankaran, R. M.; Zorman, C. A.; Feng, P. X. L. Tuning Optical Signatures of Single- and Few-Layer MoS2 by Blown-Bubble Bulge Straining up to Fracture. *Nano Lett.* **2017**, *17* (8), 4568–4575. https://doi.org/10.1021/ACS.NANOLETT.7B00730.

(13) Christopher, J. W.; Vutukuru, M.; Lloyd, D.; Bunch, J. S.; Goldberg, B. B.; Bishop, D. J.; Swan, A. K. Monolayer MoS2 Strained to 1.3% with a Microelectromechanical System. *J. Microelectromechanical Syst.* **2019**, *28* (2), 254–263. https://doi.org/10.1109/JMEMS.2018.2877983.

(14) Boddeti, N. G.; Koenig, S. P.; Long, R.; Xiao, J.; Bunch, J. S.; Dunn, M. L. Mechanics of Adhered, Pressurized Graphene Blisters. *J. Appl. Mech. Trans. ASME* **2013**, *80* (4). https://doi.org/10.1115/1.4024255.

(15) Wan, K. T.; Mai, Y. W. Fracture Mechanics of a New Blister Test with Stable Crack Growth. *Acta Metall. Mater.* **1995**, *43* (11), 4109–4115. https://doi.org/10.1016/0956-7151(95)00108-8.

(16) Dai, Z.; Rao, Y.; Lu, N. Two-Dimensional Crystals on Adhesive Substrates Subjected to Uniform Transverse Pressure. *Int. J. Solids Struct.* **2022**, *257*, 111829. https://doi.org/10.1016/J.IJSOLSTR.2022.111829.

(17) Suk, J. W.; Na, S. R.; Stromberg, R. J.; Stauffer, D.; Lee, J.; Ruoff, R. S.; Liechti, K. M. Probing the Adhesion Interactions of Graphene on Silicon Oxide by Nanoindentation. *Carbon N. Y.* **2016**, *103*, 63–72. https://doi.org/10.1016/J.CARBON.2016.02.079.

(18) Pickering, J. P.; Van Der Meer, D. W.; Vancso, G. J. Effects of Contact Time, Humidity, and Surface Roughness on the Adhesion Hysteresis of Polydimethylsiloxane. *J. Adhes. Sci. Technol.* **2012**, *15* (12), 1429–1441. https://doi.org/10.1163/156856101753213286.

(19) Greenwood, J. A.; Johnson, K. L. The Mechanics of Adhesion of Viscoelastic Solids. *Mater. Sci. Eng. R Reports* **2006**, *43* (3), 697–711. https://doi.org/10.1080/01418618108240402.

(20) Horn, R. G.; Israelachvili, J. N.; Pribac, F. Measurement of the Deformation and Adhesion of Solids in Contact. *J. Colloid Interface Sci.* **1987**, *115* (2), 480–492. https://doi.org/10.1016/0021-9797(87)90065-8.

(21) Kesari, H.; Doll, J. C.; Pruitt, B. L.; Cai, W.; Lew, A. J. Role of Surface Roughness in Hysteresis during Adhesive Elastic Contact. *Philos. Mag. Lett.* **2010**, *90* (12), 891–902. https://doi.org/10.1080/09500839.2010.521204.

(22) Schwartz, L. W.; Garoff, S. Contact Angle Hysteresis on Heterogeneous Surfaces.

Langmuir **1985**, *1* (2), 219–230. https://doi.org/10.1021/LA00062A007.